The Astrophysical Journal, 879:25 (8pp), 2019 July 1 https://doi.org/10.3847/1538-4357/ab24c8

Highly Ordered and Pinched Magnetic Fields in the Class 0 Protobinary System L1448 IRS 2

Woojin Kwon[1,2], Ian W. Stephens[3], John J. Tobin[4,5,6], Leslie W. Looney[7], Zhi-Yun Li[8], Floris F. S. van der Tak[9,10], and Richard M. Crutcher[7]

[1] Korea Astronomy and Space Science Institute (KASI), 776 Daedeokdae-ro, Yuseong-gu, Daejeon 34055, Republic of Korea; wkwon@kasi.re.kr
[2] University of Science and Technology, Korea (UST), 217 Gajeong-ro, Yuseong-gu, Daejeon 34113, Republic of Korea
[3] Harvard-Smithsonian Center for Astrophysics, 60 Garden Street, Cambridge, MA, USA
[4] National Radio Astronomy Observatory, 520 Edgemont Road, Charlottesville, VA 22903, USA
[5] Homer L. Dodge Department of Physics and Astronomy, University of Oklahoma, 440 W. Brooks Street, Norman, OK 73019, USA
[6] Leiden Observatory, Leiden University, P.O. Box 9513, 2300-RA Leiden, The Netherlands
[7] Department of Astronomy, University of Illinois, 1002 West Green Street, Urbana, IL 61801, USA
[8] Astronomy Department, University of Virginia, Charlottesville, VA 22904, USA
[9] SRON Netherlands Institute for Space Research, Landleven 12, 9747 AD Groningen, The Netherlands
[10] Kapteyn Astronomical Institute, University of Groningen, P.O. Box 800, 9700 AV Groningen, The Netherlands
Received 2018 May 18; revised 2019 April 22; accepted 2019 May 24; published 2019 July 1

Abstract

We have carried out polarimetric observations with the Atacama Large Millimeter/submillimeter Array toward the Class 0 protostellar system L1448 IRS 2, which is a protobinary embedded within a flattened, rotating structure, and for which a hint of a central disk has been suggested, but whose magnetic fields are aligned with the bipolar outflow on the cloud core scale. Our high-sensitivity and high-resolution (∼100 au) observations show a clear hourglass magnetic field morphology centered on the protostellar system, but the central pattern is consistent with a toroidal field indicative of a circumstellar disk; though, other interpretations are also possible, including field lines dragged by an equatorial accretion flow into a configuration parallel to the midplane. If a relatively large disk does exist, it would suggest that the magnetic braking catastrophe is averted in this system, not through a large misalignment between the magnetic and rotation axes, but rather through some other mechanisms, such as nonideal magnetohydrodynamic effects and/or turbulence. We have also found a relationship of decreasing polarization fractions with intensities and the various slopes of this relationship can be understood as multiple polarization mechanisms and/or depolarization from a changing field morphology. In addition, we found a prominent clumpy depolarization strip crossing the center perpendicular to the bipolar outflow. Moreover, a rough estimate of the magnetic field strength indicates that the field is strong enough to hinder formation of a rotationally supported disk, which is inconsistent with the feature of a central toroidal field. This also suggests that early disk formation can happen even in young stellar objects with a strong primordial magnetic field.

Key words: magnetic fields – stars: formation – stars: protostars – submillimeter: ISM

1. Introduction

Magnetic fields are thought to play a significant role in star formation on all scales from the cloud (∼1 pc) to the disk (∼100 au). For example, it has been found that magnetic field directions are well ordered and typically perpendicular to parsec-scale filamentary structures (e.g., Palmeirim et al. 2013), which indicates that magnetic fields are important to form such intermediate scale structures. Also, the magnetic energy is comparable to the kinetic energy down to a few thousand astronomical unit scales (e.g., Li et al. 2014; Pattle et al. 2017).

In addition, magnetic fields can affect circumstellar disk formation at the early protostellar stages. Hull et al. (2013) found that magnetic field directions of 16 young stellar objects (YSOs) are rather random with respect to their bipolar outflows on a few hundred astronomical unit scales, although a couple of examples with hourglass morphology magnetic fields aligned to its bipolar outflow had been known at the time (Girart et al. 2006; Stephens et al. 2013). Later, it was suggested that the magnetic field directions of YSOs can be understood with the existence of an extended disk structure at the youngest YSOs, the so-called Class 0 YSOs (e.g., Segura-Cox et al. 2015). For example, L1527 has a magnetic field morphology perpendicular to the bipolar outflow and has an extended Keplerian disk (radius ∼54 au; Tobin et al. 2012; Hull et al. 2013; Ohashi et al. 2014), whereas L1157, which has a magnetic field aligned with the bipolar outflow, has no disk structure larger than 15 au (Stephens et al. 2013; Tobin et al. 2013). Such features have been explained by magnetic braking, which can be so efficient in YSOs having a magnetic field aligned with the bipolar outflow that a rotation-supported disk structure is largely suppressed at the early stages (e.g., Mellon & Li 2008; Hennebelle & Ciardi 2009; Joos et al. 2012; Maury et al. 2018), often called the magnetic braking catastrophe of disk formation.

However, not all Class 0 YSOs fit the interpretation connecting the magnetic field morphology and the disk structure. For example, although a rotating disk-like structure has been detected around L1448 IRS 2 and its central binary companion (e.g., Tobin et al. 2015, 2016), the magnetic field direction detected on 500–1000 au scales is mostly aligned with the bipolar outflow (Hull et al. 2014), in which magnetic braking is expected to be efficient. In addition, Davidson et al. (2014) reported that the most preferred magnetic field for the Class 0 YSO L1527, which has a large Keplerian disk (Tobin et al. 2012; Ohashi et al. 2014), is a weak field aligned with the bipolar outflow, not a perpendicular field, when considering magnetic fields of large ∼3000 au scales as well as small

~500 au scales. On the other hand, as an example, Machida et al. (2014) reported that the magnetic braking effect depends on density distributions of the dense cores that collapse to form the YSOs as well as magnetic field morphologies. Also, it has been discussed that numerical simulations using a large sink radius suppress disk formation at the early evolutionary stages. In addition, nonideal magnetohydrodynamic (MHD) effects (e.g., ohmic dissipation, ambipolar diffusion, and Hall effect) can enable the formation of a small rotationally supported disk even in the case of a magnetic field aligned with the bipolar outflow that has efficient braking in the ideal MHD simulations (e.g., Inutsuka et al. 2010; Krasnopolsky et al. 2011; Dapp et al. 2012; Tomida et al. 2015; Tsukamoto et al. 2015; Zhao et al. 2018).

An obvious way to investigate whether primordial magnetic field morphologies affect disk formation at the early evolutionary stages is to examine the small scale fields of those YSOs that have envelope-scale (1000–10,000 au) fields aligned with the bipolar outflow. In this paper, we report polarimetric observations of the Atacama Large Millimeter/submillimeter Array (ALMA) toward L1448 IRS 2 focusing on how the magnetic fields change on 100 au scales.

2. Target and Observations

Several Class 0 YSOs with flattened envelope structures have been identified by Tobin et al. (2010) in the Perseus molecular cloud at a distance of about 300 pc (Ortiz-León et al. 2018; Zucker et al. 2018). Of these envelopes, L1448 IRS 2 has the clearest flattened structure and has been observed in polarization indicating a magnetic field aligned with the bipolar outflow (Hull et al. 2014). Previous studies have imaged a large, extended bipolar outflow originating from the target at various wavelengths: e.g., near-IR observations using the *Spitzer Space Telescope* (Tobin et al. 2007). In addition, Kwon et al. (2009) reported that grains have significantly grown based on the dust opacity spectral index estimated from 1 and 3 mm observations of the Combined Array for Research in Millimeter-wave Astronomy (CARMA). Regarding polarimetric observations, Caltech Submillimeter Observatory SHARP observations detected 350 μm continuum polarization perpendicular (inferred magnetic field[11] parallel) to the bipolar outflow with a 10″ angular resolution (Chapman et al. 2013). Hull et al. (2014) also detected polarization in the same direction, particularly in the blueshifted lobe on the northwest side from the center with an angular resolution of ~2″.

Polarimetric observations toward L1448 IRS 2 in ALMA Band 6 were made on 2016 November 12 and 14 (2016.1.00604.S, PI: Woojin Kwon). Individual tracks were run over 3 hr to achieve a good parallactic angle coverage. HH 211 was observed simultaneously with L1448 IRS 2 and shared the same phase calibrator; HH 211 will be reported in a separate paper. The November 12 and 14 tracks have 42 and 40 antennas in the array, respectively. J0238+1636 was used as polarization calibrator and flux calibrator. Its flux was set to 1.085 Jy at 233 GHz with a spectral index of about −0.45. J0237+2848 and J0336+3218 were bandpass and phase calibrators, respectively. All the execution blocks were calibrated separately and combined when making images. Images were made using a Brigg's weighting with a robust parameter of 0.5. We found that this weighting was a good compromise between resolution and sensitivity. The final image has a synthesized beam of 0.″57 × 0.″37 (PA = 9.°14). The noise levels of Stokes I (total intensity), Q, and U maps are ~0.10, ~0.014, and ~0.014 mJy beam^{-1}, respectively. The polarization intensity map achieved by the Stokes Q and U maps with a debias using the Stokes Q and U map noise level has an rms noise of 0.008 mJy beam^{-1}.

[11] Assuming magnetic field grain alignment, the magnetic field directions are inferred by 90° rotation of polarization directions.

3. Results

3.1. Magnetic Field Morphology

Magnetic fields are inferred perpendicular to polarizations of dust thermal emission in millimeter/submillimeter wavelengths, because nonspherical dust grains are aligned with their minor axes (spin axes) parallel to magnetic fields (e.g., Lazarian & Hoang 2007). In Figure 1, we rotate the polarization directions by 90° and infer the magnetic fields. The magnetic field morphology shows a beautifully clear hourglass morphology perpendicular to the elongated structure. Consistent with previous CARMA observations (Hull et al. 2014), the region northwest of the center shows a poloidal field, which is approximately aligned with the bipolar outflow direction. However, in the central region the field direction rapidly changes to an orientation perpendicular to the bipolar outflow, which is consistent with the polarization pattern produced by grains aligned with a toroidal magnetic field close to the protostar.

Recently, however, it has also been reported that magnetic fields on disk scales cannot be inferred from polarization patterns because other polarization mechanisms may be dominant. Kataoka et al. (2017) and Stephens et al. (2017b) showed that polarization of dust thermal emission in HL Tau dramatically changes with wavelengths. In Band 3 (3 mm) the polarization pattern is azimuthal, which may be understood by anisotropic radiation alignment (Tazaki et al. 2017; Yang et al. 2019), while in Band 7 (0.85 mm) it is parallel to the disk minor axis, which is indicative of scattering. For the intermediate wavelength, Band 6 (1.3 mm), the pattern is a combination of the two. These results indicate that polarization may not be able to probe magnetic fields. In contrast, Alves et al. (2018) found that the Class I YSO BHB07-11 has a uniform polarization pattern over Bands 3, 6, and 7 of ALMA. This suggests that dust grains are not large, and that they are aligned with magnetic fields. On the other hand, Liu et al. (2018) addressed that polarizations can be caused by extinction even in millimeter wavelengths, particularly toward high optical depth regions having temperature increasing with distance from the observer along the line of sight. In such cases, polarization fractions could be high (several percent or larger depending on optical depth and background and foreground temperatures), and magnetic fields are inferred parallel to the polarization direction, unlike the usual case of polarizations in the thermal dust emission of (sub)millimeter wavelengths.

With our data set taken in Band 6 toward the Class 0 YSO L1448 IRS 2, which is discussed in this paper, we argue that the polarizations come from dust grains aligned with magnetic fields. Regarding the central region, other polarization mechanisms are worth discussing. First, based on the polarization pattern at the center, with E-vectors parallel to the bipolar outflow, it is unlikely caused by alignment of anisotropic

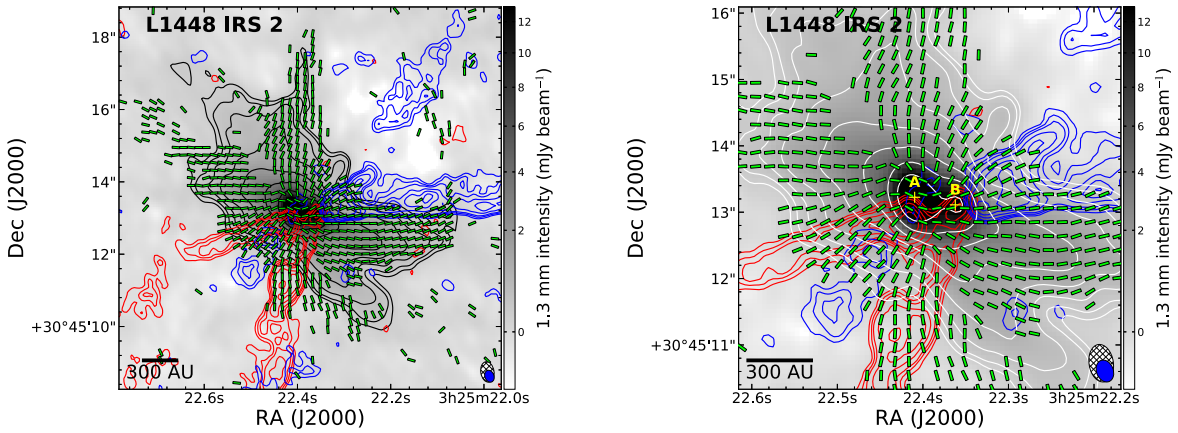

Figure 1. Magnetic field morphology around L1448 IRS 2. The green vectors have been rotated by 90° from the polarization directions to indicate the inferred magnetic field direction. Vectors of 2σ level or better detections are marked every 0.″21, which is comparable to the Nyquist sampling. The gray scale and black and white contours present the total intensity distribution with levels of 2, 3, 5, 9, 17, 33, 65, and 129 times 0.1 mJy beam^{-1}. The blue and red contours are CO 2–1 intensity distributions integrated in velocity ranges of −8.0 to 2.0 and 7.5 to 16.0 km s^{-1}, respectively, at levels of 3, 4, 5, 7, and 9 times 11 K km s^{-1}. The central region zoomed-in is presented on the right. The synthesized beams of the CO and the continuum data are marked in the bottom right corner in blue and hatched white, respectively. The binary system positions are 2A(03:25:22.407 +30:45:13.21) and 2B(03:25:22.363 +30:45:13.12) in J2000.

radiation. Also, the intensity peak is about 26 mJy beam^{-1}, which corresponds to an optical depth $\tau \sim 0.2$ when assuming $T = 30$ K, so the polarization may not be caused by extinction. Therefore, the magnetic fields may be inferred by 90° rotation of polarization directions, which results in a pattern in the central region that is broadly consistent with a toroidal magnetic field projected in the sky plane. On the other hand, self-scattering cannot be ruled out by the data set taken only in Band 6. However, note that even in this case, it may provide indirect evidence for the presence of a circumstellar disk(-like) structure at the center, since self-scattering has been found so far only toward disks with large grains. Therefore, the main result of this paper does not change. The ambiguity will be tackled by further polarimetric observations in different wavelengths. Indeed, we have carried out polarimetric observations in ALMA Band 3 as well, and the preliminary results support the interpretation of magnetic fields. These results will be discussed in a following paper (W. Kwon et al. 2019, in preparation).

In addition, there is the possibility that the central polarization pattern is produced by magnetic field lines that are dragged by an equatorial accretion flow into a configuration that is parallel to the midplane of the system. However, we believe this possibility is less likely than the rotationally induced toroidal field interpretation because there is already evidence for significant velocity gradient along the equatorial plane (see, e.g., Figure 11 of Tobin et al. 2018). Nevertheless, higher resolution line observations are needed to firmly establish whether the intriguing field orientation near the center is produced by accretion or rotation. Note the seven vectors around the source A within or on the inner most contour in the right zoomed-in plot of Figure 1. A detailed modeling may be required to constrain the structure size of a toroidal magnetic field. However, based on the number of vectors showing the shifted direction, which is 1.5 of the beam area, the central disk could be up to about 50 au in radius: considering a beam smoothing, the real structure would be about 0.5 of the beam area, so $r = (0.5A_{\rm beam}/\pi)^{0.5}d$, where $A_{\rm beam}$ is the beam area and d is the target distance. Further molecular line observations at a high angular resolution will provide the information on how large the disk is, if it existed, and whether it is rotationally supported.

Note that the self-scattering polarization pattern is expected to be parallel to the minor axis of an inclined disk (e.g., Yang et al. 2016; Kataoka et al. 2017; Stephens et al. 2017b), which means that after a 90° rotation, the corresponding B vectors look like a toroidal feature. If the toroidal field interpretation is correct, it would indicate that rotation has become fast and energetic enough to wind up the field lines, which likely signals the formation of a rapidly rotating disk. If the dust self-scattering interpretation is correct, it would indicate that grains in the flattened structure on the scale of several tens of astronomical units have grown to roughly 100 μm sizes or more, which again would favor the existence of a rotationally supported disk that is conducive to grain growth through a higher density and longer time compared to a dynamically collapsing inner envelope. Recently, some other ALMA polarimetric observations have also presented polarization patterns of self-scattering or toroidal magnetic fields in the central regions of Class 0 and I YSOs with a disk (Lee et al. 2018; Sadavoy et al. 2018) and disk candidates (Cox et al. 2018). Additional polarimetric observations at different wavelengths will allow us to distinguish magnetic field alignment from self-scattering (e.g., Alves et al. 2018, Kwon et al. 2019, in preparation).

The contours in the right panel of Figure 1 also show the binary companion (L1448 IRS 2B), which is separated from the primary by about 0.″6 (corresponding to ∼180 au at the target distance) toward the west. This companion is less bright in the 1 mm continuum and has been detected at 9 mm (*Ka*-band; Tobin et al. 2016) and at 1 mm (Tobin et al. 2018). The blue and red contours overlaid in the figure are CO 2–1 molecular line data taken by ALMA (2013.1.00031.S; Tobin et al. 2018). The angular resolution of the CO 2–1 observations is 0.″35 × 0.″25 (PA: 21°), which is slightly better than the polarimetric continuum data. Since these observations lack short baselines, only the cavity walls were detected, as the extended features between the walls (as detected in Tobin et al. 2015) are filtered out. Interestingly, the less bright companion L1448 IRS 2B seems to be more coincident with the bipolar

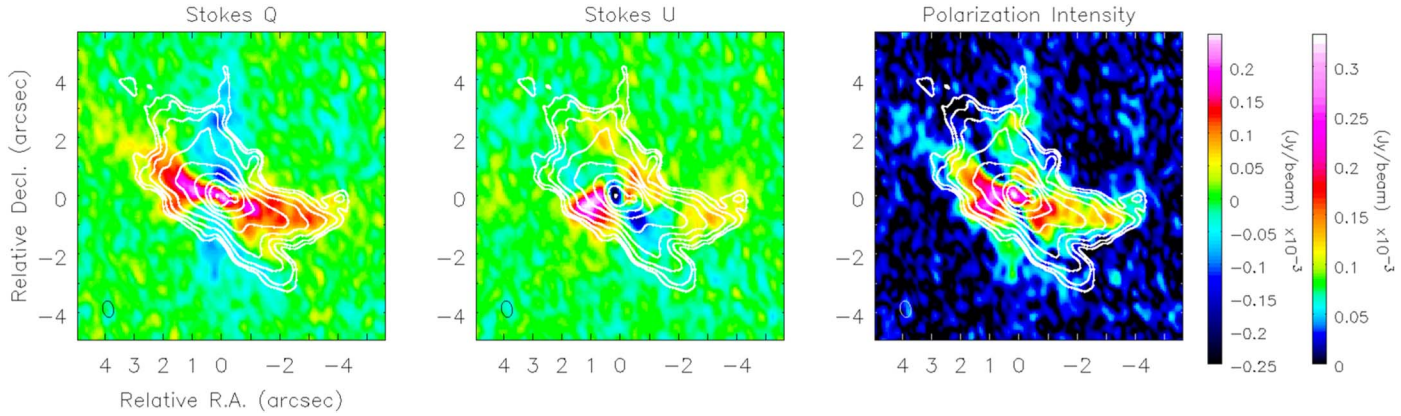

Figure 2. Stokes Q, Stokes U, and polarization intensity maps are on the left, in the middle, and on the right, respectively. The contours present distributions of total intensity (Stokes I) at the same levels of Figure 1. The color edges are for the Stokes Q and U maps (the left covering minus and plus values) and the polarization intensity map (the right).

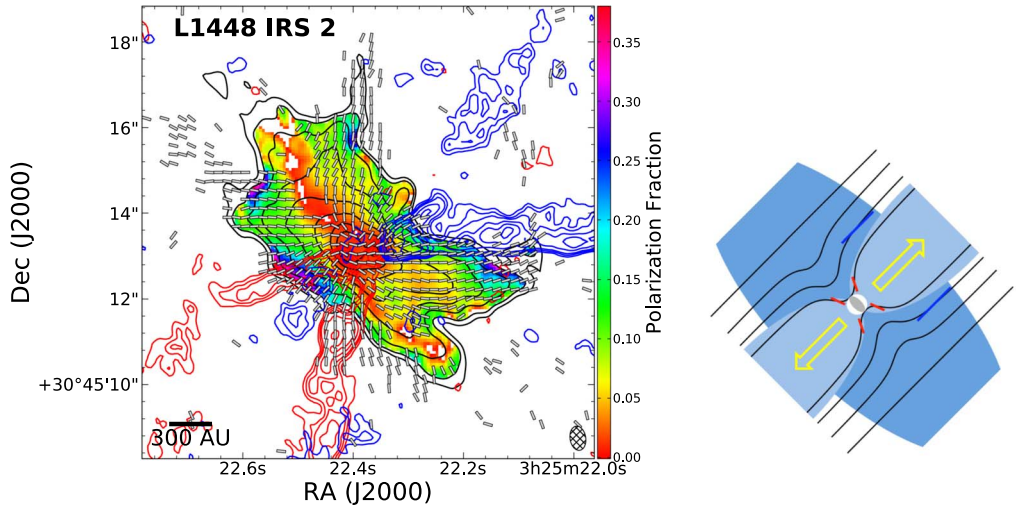

Figure 3. Polarization fraction distribution indicated in color scales. The other plot components are the same as those in Figure 1. The schematic diagram on the right illustrates hourglass morphology magnetic fields detected in different alignment: small scales in red and large scales in blue.

outflow. While the redshifted lobe is primarily centered on the combination of both L1448 IRS 2A and 2B, the main blueshifted lobe seems to be centered on L1448 IRS 2B only. However, there is a weak blueshifted feature from the L1448 IRS 2A and along the left continuum branch. It is possible that the blueshifted component from L1448 IRS 2A might be in the same velocity regime of the ambient cloud and thus could be filtered out by the interferometer.

3.2. Polarization Intensity and Fraction

In Figure 2, the outflow cavity walls have relatively high polarization intensities, while there is a strip across the center, almost perpendicular (P.A. $\sim$35°) to the bipolar outflow (P.A. $\sim$ 118° at large scales; Stephens et al. 2017a), with weak polarization signal lower than a few tens μJy beam^{-1}. This depolarized strip is shown in more detail in Figure 3 and discussed below. The polarization intensity is not symmetrically distributed. The central region of the total intensity peak has the highest polarization intensity. Also, the region south of the depolarized strip to the east of the center is high in polarization intensity. In addition, polarization intensity is very clumpy compared to the total intensity distributions, which is indicative that polarization is significantly affected by the local environment.

As shown in Figure 3, the depolarization regions of L1448 IRS 2 clearly appear at the central region and along the strip perpendicular to the bipolar outflow, whose polarization fractions are only a few percent or less. The central region with the binary system presumably has the most complicated magnetic fields. Also, as addressed, the magnetic fields are changing from aligned to perpendicular with respect to the bipolar outflow going from large to small scales. These complicated polarization patterns that are smaller than the beam reduce the measured polarization fraction: i.e., beam smearing. A complicated magnetic field could also be caused by turbulence (e.g. Hull et al. 2017). However, in the case of the turbulence-induced, depolarized regions are rather randomly distributed (Lee et al. 2017).

On the other hand, the depolarized strip is similar to the case of an inclined cloud with an hourglass-shaped magnetic field (Kataoka et al. 2012). Indeed, Tobin et al. (2007) reported that the bipolar outflow is inclined by about 57° (where 90° indicates a bipolar outflow on the sky plane). The inferred inclination makes it possible for the radially pinched field lines along a given line of sight to produce polarizations that cancel one another, yielding a less polarized equatorial region (see Figure 6(d) of Kataoka et al. 2012). Furthermore, rotation of a cloud introduces a misalignment to the depolarized strip (see

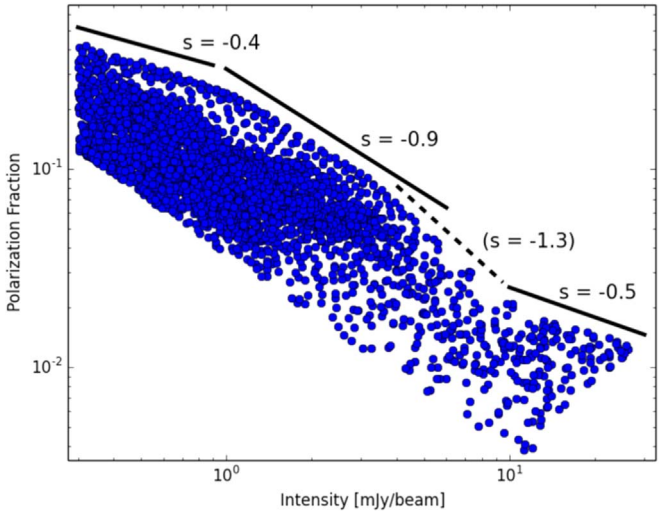

Figure 4. Polarization fraction vs. intensity. Each blue circle represents a pixel value, and the black lines indicate individual power-law slopes, not fitting results. Data points of intensities greater than 3σ and polarization intensities larger than 2σ have been selected.

Figure 10(d) of Kataoka et al. 2012), which is broadly consistent with the depolarized feature shown in Figure 3.

Depolarization can also occur due to high optical depth (see Figure 3 of Yang et al. 2017), but this is not likely the case here since the optical depth is expected to be low along this depolarization strip: $\tau \sim 0.08$ even at the highest contour level assuming $T = 30$ K.

In addition, along the depolarized strip, there are several depolarized clumps, whose sizes are not resolved at our angular resolution, as seen in the white space in Figure 3. The clumps are separated by $\sim 0\farcs8$, which corresponds to about 240 au at the distance of Perseus. These clumps may indicate relatively more turbulent areas with chaotic magnetic fields and/or areas with magnetic fields pointing along the line-of-sight direction. They may even be demagnetized "islands" produced by reconnection of sharply pinched magnetic field lines (see Figure 7 of Suriano et al. 2017); though, detailed exploration of magnetic reconnection is beyond the scope of this paper.

The highest polarization fractions, reaching levels of up to 40%, are located near the border of the northwest and southeast part of the envelope. Such high polarization fractions can occur only by very elongated, aligned dust grains (e.g., axis ratios larger than 3; Lee & Draine 1985). Based on the high polarization fraction locations, we speculate that mechanical alignment could also contribute to the polarization in the cavity walls. In the case of mechanical alignment, it has recently been suggested that the spinning, minor axis of elongated dust grains are aligned with the mechanical flow (Hoang et al. 2018), in contrast to the classical mechanical alignment (Gold 1952). Therefore, the polarization directions could be the same as the dust grains aligned in poloidal magnetic fields along the bipolar outflow.

Nevertheless, the largest origin of the high polarization fractions would be the differential filtering in Stokes maps. The continuum structure is more extended in Stokes I than those in Stokes Q and U, as shown in Figure 2. This results in more flux of Stokes I being filtered out, which significantly contributes to the high polarization fractions, particularly at the edges.

Figure 4 shows decreasing polarization fractions ($P_{\rm frac}$) with Stokes I intensities (I) overall. This trend has been reported by many previous polarimetric observations of arcseconds (e.g., Girart et al. 2006; Kwon et al. 2006; Liu et al. 2013; Hull et al. 2014; Galametz et al. 2018) and tens arcseconds or coarser angular resolutions (e.g., Dotson 1996; Collaboration et al. 2016; Soam et al. 2018). Going toward a central denser region, dust grains get larger causing less alignment in a magnetic field, optical depth increases, and/or magnetic fields likely become complicated, which all result in a lower polarization fraction. Note that dust grains getting larger, such as above 10 μm in disk conditions, cause less alignment with the magnetic field because the Larmor precession rate becomes slower than the gas randomization rate (Hoang & Lazarian 2016; Tazaki et al. 2017).

Regarding power-law indices of the relationship, when polarized emission is dominated from the surface of a structure, the polarization fraction is expected to be inversely proportional to the intensity in the optically thin case ($P_{\rm frac} \propto I^{-1}$): e.g., polarization caused by dust grains aligned by magnetic fields due to the interstellar radiative torque (RAT, Lazarian & Hoang 2007) mainly around the molecular cloud surface. Interestingly, Figure 4 shows multiple slopes that encompass the limits of the distributions in a qualitative manner. In the regime fainter than about 1 mJy beam^{-1}, the slope is roughly -0.4. This region corresponds to the area from the second lowest contour to about the fourth contour in the 1 mm continuum map of Figure 3. The slope shallower than -1 could be interpreted with additional polarization contributions from these areas (as addressed above, e.g., mechanical alignment), not limited to just the structure surface. Between $\sim$1 and $\sim$10 mJy beam^{-1}, the slope is close to -1, which is indicative that the regions have no further significant polarization. Approaching the 10 mJy beam^{-1}, the slope becomes a little bit steeper than -1: $s = -1.3$. This can be interpreted as polarization directions changing, resulting in depolarization. Indeed, the region is where the field directions switch from the poloidal to the toroidal pattern. For the central region that is brighter than 10 mJy beam^{-1} the slope is -0.5. This shallower slope than -1 may be caused by grain alignment closer to a central star through RAT, although it would be less efficient compared to the case of outer fine grains. In addition, presumably self-scattering of emission from large grains may also contribute to the polarization fraction at these scales (e.g., Kataoka et al. 2017; Stephens et al. 2017b, 2014), although it may not be dominant in this target.

4. Discussion

4.1. Magnetic Field Strength

We estimate a very rough magnetic field strength using the Davis–Chandrasekhar–Fermi (DCF) method (Davis 1951; Chandrasekhar & Fermi 1953). We are aware that the field orientations can be affected by outflows and gravitational collapse near a protostellar system, which will likely degrade the accuracy of the DCF method, but quantifying such effects would require more detailed dynamical modeling that is beyond the scope of this paper. In the DCF technique, the magnetic field strength is estimated based on the dispersion of magnetic fields with respect to the background field direction compared to its turbulence in a given density medium. In other

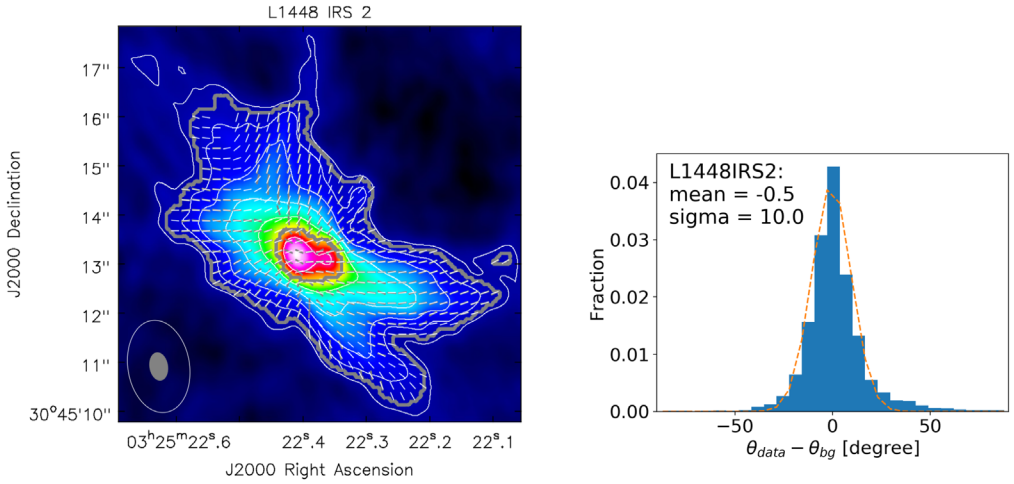

Figure 5. Intensity map in color scales. Magnetic fields of the original angular resolution are marked in gray and fields smoothed by nine times larger beams in area are in white. Refer to the text for the thick gray contour lines. In the right is the histogram of the magnetic field directions with respect to the background field.

words, a medium at a given density and a turbulence indicated by a nonthermal linewidth would have a stronger magnetic field strength when it has a smaller field position angle dispersion: the plane-of-sky strength of a magnetic field $B_{\rm POS} = Q\sqrt{4\pi\rho}\ \delta V/\delta\phi \approx 9.3\sqrt{n({\rm H_2})}\,\Delta V/\delta\phi$ [μG], where Q, ρ, δV, $\delta\phi$, and $n(H_2)$ are a factor of order unity, the gas density, the nonthermal velocity dispersion in km s^{-1}, the position angle dispersion of polarizations, and the molecular hydrogen number density, respectively (e.g., Ostriker et al. 2001; Crutcher et al. 2004).

First, for the background large-scale fields we smoothed the Stokes Q and U maps with a nine-times larger beam (extended in both major and minor axes of the original beam by a factor of three), which is comparable to half of the width across the continuum structure. This provides a reasonable background field morphology (Pattle et al. 2017). As Figure 5 shows, the smoothed fields in white vectors do not show the toroidal switch at the central region. Since we know the central area is confused by the morphological change in scales and with evolution and possible polarization contamination from scattering, we only apply the DCF method to the areas between intensities of 0.3 and 6.5 mJy beam^{-1} (thick gray contours in Figure 5), for estimating the magnetic field strength. The measured dispersion is estimated as 10° (Figure 5, right). Second, for estimating the number density of H_2 we utilized the dust continuum. The total continuum flux density of the area between 0.3 and 6.5 mJy beam^{-1}, which is 18.2 squared arcseconds, is about 91 mJy at 233 GHz. The total mass is estimated by $M_T = F_\nu D^2/\kappa_\nu B_\nu(T_d)$, where F_ν, D, κ_ν, B_ν, and T_d are the flux density, distance, mass absorption coefficient, blackbody radiation intensity, and dust temperature, respectively. Using $F_\nu = 91$ mJy, $D = 300$ pc, and $\kappa_\nu = 0.01$ cm^2 g^{-1} at 233 GHz (Ossenkopf & Henning 1994) assuming a gas-to-dust mass ratio of 100, and $T_d = 30$ K (Kwon et al. 2009), the total mass is estimated to be 0.08 $M_\odot$. In addition, assuming a cylinder with the profile of the continuum feature, the total volume would be 9×10^{48} cm^3. Therefore, we derive the volume density $\rho \approx 1.8 \times 10^{-17}$ g cm^{-3}, which corresponds to $n(H_2) \approx 5.3 \times 10^6$ cm^{-3}. We do not have an observational nonthermal linewidth, but it may be reasonable to adopt the trans-sonic velocity at 30 K: ~0.3 km s^{-1}. These values result in the magnetic field strength in the plane of the sky of about 640 μG, with the relationship following:

$$B_{\rm POS} \approx 640\ \mu{\rm G}\left(\frac{n({\rm H_2})}{5.3\times10^6\ {\rm cm^{-3}}}\right)^{0.5}\left(\frac{\Delta V}{0.3\ {\rm km\ s^{-1}}}\right)\left(\frac{10^\circ}{\delta\phi}\right). \quad (1)$$

Furthermore, we estimate the magnetic braking timescale of the presumed disk structure at the center, when the rotation velocity decreases by half (e.g., Basu & Mouschovias 1994). The Alfvén speed follows the relationship,

$$v_A = \frac{B}{\sqrt{4\pi\rho}} = 0.43\ {\rm km\ s^{-1}}\left(\frac{B}{640\ \mu{\rm G}}\right)\left(\frac{1.8\times10^{-17}\ {\rm g\ cm^{-3}}}{\rho}\right)^{0.5}. \quad (2)$$

In addition, the central mass surrounded by the inner thick gray contour in Figure 5 is estimated as 0.05 $M_\odot$ based on the total flux density of 55 mJy. This mass is rather uncertain: it could be overestimated because the central region is warmer than the outer region and could be underestimated because the very central region (< a few astronomical units in radius) would be optically thick even in millimeter wavelengths. On the other hand, the central rotating structure could be much smaller than the inner region considered here. The same mass beyond the central area is extended up to the intensity of ~1.1 mJy beam^{-1}, which is about 0.″5 (150 au) away. When the Alfvén wave reaches this point, the rotating mass tied up by the magnetic field is doubled so the rotation velocity becomes a half, assuming angular momentum conservation. This timescale is calculated to be ~1700 yr. Note that this is much shorter than the typical age of Class 0 YSOs, which is several thousand years. Furthermore, when regarding the canonical accretion rate of Class 0 YSOs ~10^{-6} $M_\odot$ yr^{-1} (e.g., Shu 1977; Dunham et al. 2014), the magnetic braking effect, which slows down 0.05 $M_\odot$ in 1700 yr, dominates the system. Taken at face value, the estimated field strength is high enough for the magnetic field to brake the disk rotation efficiently. However, as we mentioned earlier, the polarization orientations on the several tens of astronomical units

scale are indicative of a disk. If true, the existence of a relatively large disk in the presence of a strong inferred magnetic field would point to a decoupling of the field from the bulk disk material, most likely through nonideal MHD effects, which become more important at higher densities (e.g., Inutsuka et al. 2010; Krasnopolsky et al. 2011; Dapp et al. 2012; Tomida et al. 2015; Tsukamoto et al. 2015; Zhao et al. 2018).

5. Conclusion

We have detected a well-ordered polarization pattern toward the Class 0 YSO L1448 IRS 2, whose inferred magnetic field presents the clearest hourglass morphology to date on 100 au scales: poloidal in the outer regions and rapidly switching to toroidal in the inner region. This can be interpreted as a toroidal magnetic field wrapped up by a rotating (disk) structure or by a self-scattered polarization pattern due to large grains in an inclined disk: either case supports a rotationally dominant structure. Future high resolution molecular line observations are needed to investigate whether there is a rotationally supported disk.

We found four regimes with different slopes in the relationship between polarization fractions and intensities, which provide interesting constraints on grain alignment mechanisms. In addition, we detected a clumpy depolarization strip, which is indicative of magnetically channeled protostellar accretion flows that drag the field lines into a radially pinched configuration and that, when combined with inclination effects, lower the degree of polarization.

Finally, we estimated the plane-of-sky magnetic field strength using the DCF technique and found that magnetic braking should be very efficient in the system, which is inconsistent with the strong hints of a central disk, protobinary, and observations of rotation. Therefore, the magnetic braking catastrophe based on simple ideal MHD simulations may not be so disastrous, at least in this source. Our observations emphasize that nonideal MHD effects (and possibly turbulence) should be taken into account, in order to fully understand the formation of disks at the early protostellar systems.

We are grateful to ALMA staff for their dedicated work and an anonymous referee for helpful comments. W.K. thanks Thiem Hoang for fruitful discussions on grain alignments and polarization mechanisms. W.K. was supported by Basic Science Research Program through the National Research Foundation of Korea (NRF-2016R1C1B2013642). J.J.T. was supported by grant 639.041.439 from the Netherlands Organisation for Scientific Research (NWO). Z.-Y.L. is supported in part by NSF AST-1313083 and AST-1716259 and NASA NNX14AB38G and 80NSSC18K1095. This paper makes use of the following ALMA data: ADS/JAO.ALMA#2016.1.00604.S, ADS/JAO.ALMA#2013.1.00031.S. ALMA is a partnership of ESO (representing its member states), NSF (USA) and NINS (Japan), together with NRC (Canada), MOST and ASIAA (Taiwan), and KASI (Republic of Korea), in cooperation with the Republic of Chile. The Joint ALMA Observatory is operated by ESO, AUI/NRAO, and NAOJ.

Facility: ALMA.

ORCID iDs

Woojin Kwon https://orcid.org/0000-0003-4022-4132
Ian W. Stephens https://orcid.org/0000-0003-3017-4418
John J. Tobin https://orcid.org/0000-0002-6195-0152
Leslie W. Looney https://orcid.org/0000-0002-4540-6587

References

Alves, F. O., Girart, J. M., Padovani, M., et al. 2018, A&A, 616, A56
Basu, S., & Mouschovias, T. C. 1994, ApJ, 432, 720
Chandrasekhar, S., & Fermi, E. 1953, ApJ, 118, 113
Chapman, N., Davidson, J., Goldsmith, P. F., et al. 2013, ApJ, 770, 151
Collaboration, P., Ade, P. A. R., Aghanim, N., et al. 2016, A&A, 586, A136
Cox, E. G., Harris, R. J., Looney, L. W., et al. 2018, ApJ, 855, 92
Crutcher, R. M., Nutter, D. J., Ward-Thompson, D., & Kirk, J. M. 2004, ApJ, 600, 279
Dapp, W. B., Basu, S., & Kunz, M. W. 2012, A&A, 541, A35
Davidson, J. A., Li, Z. Y., Hull, C. L. H., et al. 2014, ApJ, 797, 74
Davis, L. 1951, PhRv, 81, 890
Dotson, J. L. 1996, ApJ, 470, 566
Dunham, M. M., Stutz, A. M., Allen, L. E., et al. 2014, in Protostars and Planets VI, ed. H. Beuther et al. (Tucson, AZ: Univ. Arizona Press), 195
Galametz, M., Maury, A., Girart, J. M., et al. 2018, A&A, 616, A139
Girart, J. M., Rao, R., & Marrone, D. P. 2006, Sci, 313, 812
Gold, T. 1952, MNRAS, 112, 215
Hennebelle, P., & Ciardi, A. 2009, A&A, 506, L29
Hoang, T., Cho, J., & Lazarian, A. 2018, ApJ, 852, 129
Hoang, T., & Lazarian, A. 2016, ApJ, 831, 159
Hull, C. L. H., Mocz, P., Burkhart, B., et al. 2017, ApJL, 842, L9
Hull, C. L. H., Plambeck, R. L., Bolatto, A. D., et al. 2013, ApJ, 768, 159
Hull, C. L. H., Plambeck, R. L., Kwon, W., et al. 2014, ApJS, 213, 13
Inutsuka, S.-i., Machida, M. N., & Matsumoto, T. 2010, ApJL, 718, L58
Joos, M., Hennebelle, P., & Ciardi, A. 2012, A&A, 543, A128
Kataoka, A., Machida, M. N., & Tomisaka, K. 2012, ApJ, 761, 40
Kataoka, A., Tsukagoshi, T., Pohl, A., et al. 2017, ApJL, 844, L5
Krasnopolsky, R., Li, Z.-Y., & Shang, H. 2011, ApJ, 733, 54
Kwon, W., Looney, L. W., Crutcher, R. M., & Kirk, J. M. 2006, ApJ, 653, 1358
Kwon, W., Looney, L. W., Mundy, L. G., Chiang, H.-F., & Kemball, A. J. 2009, ApJ, 696, 841
Lazarian, A., & Hoang, T. 2007, MNRAS, 378, 910
Lee, C.-F., Li, Z.-Y., Ching, T.-C., Lai, S.-P., & Yang, H. 2018, ApJ, 854, 56
Lee, H. M., & Draine, B. T. 1985, ApJ, 290, 211
Lee, J. W. Y., Hull, C. L. H., & Offner, S. S. R. 2017, ApJ, 834, 201
Li, H.-b., Goodman, A., Sridharan, T. K., et al. 2014, in Protostars and Planets VI, ed. H. Beuther et al. (Tucson, AZ: Univ. Arizona Press), 101
Liu, H. B., Hasegawa, Y., Ching, T.-C., et al. 2018, A&A, 617, A3
Liu, H. B., Qiu, K., Zhang, Q., Girart, J. M., & Ho, P. T. P. 2013, ApJ, 771, 71
Machida, M. N., Inutsuka, S.-i., & Matsumoto, T. 2014, MNRAS, 438, 2278
Maury, A. J., Girart, J. M., Zhang, Q., et al. 2018, MNRAS, 477, 2760
Mellon, R. R., & Li, Z.-Y. 2008, ApJ, 681, 1356
Ohashi, N., Saigo, K., Aso, Y., et al. 2014, ApJ, 796, 131
Ortiz-León, G. N., Loinard, L., Dzib, S. A., et al. 2018, ApJ, 865, 73
Ossenkopf, V., & Henning, T. 1994, A&A, 291, 943
Ostriker, E. C., Stone, J. M., & Gammie, C. F. 2001, ApJ, 546, 980
Palmeirim, P., André, P., Kirk, J., et al. 2013, A&A, 550, A38
Pattle, K., Ward-Thompson, D., Berry, D., et al. 2017, ApJ, 846, 122
Sadavoy, S. I., Myers, P. C., Stephens, I. W., et al. 2018, ApJ, 859, 165
Segura-Cox, D. M., Looney, L. W., Stephens, I. W., et al. 2015, ApJL, 798, L2
Shu, F. H. 1977, ApJ, 214, 488
Soam, A., Pattle, K., Ward-Thompson, D., et al. 2018, ApJ, 861, 65
Stephens, I. W., Dunham, M. M., Myers, P. C., et al. 2017a, ApJ, 846, 16
Stephens, I. W., Looney, L. W., Kwon, W., et al. 2013, ApJL, 769, L15
Stephens, I. W., Looney, L. W., Kwon, W., et al. 2014, Natur, 514, 597
Stephens, I. W., Yang, H., Li, Z.-Y., et al. 2017b, ApJ, 851, 55
Suriano, S. S., Li, Z.-Y., Krasnopolsky, R., & Shang, H. 2018, MNRAS, 477, 1239
Tazaki, R., Lazarian, A., & Nomura, H. 2017, ApJ, 839, 56
Tobin, J. J., Chandler, C. J., Wilner, D. J., et al. 2013, ApJ, 779, 93
Tobin, J. J., Hartmann, L., Chiang, H.-F., et al. 2012, Natur, 492, 83
Tobin, J. J., Hartmann, L., Looney, L. W., & Chiang, H.-F. 2010, ApJ, 712, 1010
Tobin, J. J., Looney, L. W., Li, Z.-Y., et al. 2016, ApJ, 818, 73
Tobin, J. J., Looney, L. W., Li, Z.-Y., et al. 2018, ApJ, 867, 43
Tobin, J. J., Looney, L. W., Mundy, L. G., Kwon, W., & Hamidouche, M. 2007, ApJ, 659, 1404
Tobin, J. J., Looney, L. W., Wilner, D. J., et al. 2015, ApJ, 805, 125

Tomida, K., Okuzumi, S., & Machida, M. N. 2015, ApJ, 801, 117
Tsukamoto, Y., Iwasaki, K., Okuzumi, S., Machida, M. N., & Inutsuka, S. 2015, ApJL, 810, L26
Yang, H., Li, Z.-Y., Looney, L. W., Girart, J. M., & Stephens, I. W. 2017, MNRAS, 472, 373
Yang, H., Li, Z.-Y., Stephens, I. W., Kataoka, A., & Looney, L. 2019, MNRAS, 483, 2371
Yang, H., Li, Z. Y., & the, L. L. M. N. o. 2016, MNRAS, 456, 2794
Zhao, B., Caselli, P., Li, Z.-Y., & Krasnopolsky, R. 2018, MNRAS, 473, 4868
Zucker, C., Schlafly, E. F., Green, G. M., et al. 2018, ApJ, 869, 83